Properties of PSCs and cirrus determined from AVHRR data

Mark Hervig
Department of Atmospheric Science, University of Wyoming, Laramie
Kathy Pagan
Geosciences Department, San Francisco State University
Patricia G. Foschi
Romberg Tiburon Center for Environmental Studies, San Francisco State University

Abstract. Polar stratospheric clouds (PSCs) and cirrus have been investigated using thermal emission measurements at 10.8 and 12 μm wavelength (channels 4 and 5) from the Advanced Very High Resolution Radiometer (AVHRR). The AVHRR signal was evaluated from a theoretical basis to understand the emission from clear and cloudy skies, and models were developed to simulate the AVHRR signal. Signal simulations revealed that nitric acid PSCs are invisible to AVHRR, while ice PSCs and cirrus are readily detectable. Methods were developed to retrieve cloud optical depths, average temperatures, average effective radii, and ice water paths, from AVHRR channels 4 and 5. Properties of ice PSCs retrieved from AVHRR were compared to values derived from coincident radiosondes and from the Polar Ozone and Aerosol Measurement II instrument, showing good agreement.

1. Introduction

This work explores the detection of polar stratospheric clouds (PSCs) and cirrus using measurements from the Advanced Very High Resolution Radiometer (AVHRR). Interests in cirrus include their role in radiative forcing of the climate system and their role in the chemical balance of the atmosphere [e.g., *Sassen et al.*, 1989; *Borrmann et al.*, 1996]. Because cirrus usually occur below the spontaneous freezing temperature of water, they are typically composed of ice crystals *Jensen et al.*, 1994]. PSCs have been implicated as key factors in the loss of ozone under cold polar conditions. Observational and theoretical evidence suggests that PSCs can be composed of either liquid ternary H_2SO_4–H_2O–HNO_3 aerosols (LTA), nitric acid trihydrate (NAT), or ice [e.g., *Tolbert*, 1996; *Carslaw et al.*, 1994].

AVHRR measures reflected and/or emitted radiation at nadir ($\pm 50°$) in five spectral bands between 0.58 and 12.5 μm wavelength (λ). A series of AVHRR sensors on board polar–orbiting satellites have been collecting data since 1979, and provide excellent temporal and spatial coverage of the polar regions. Poleward of 60°, each point on the earth's surface is sampled in two or more consecutive passes twice a day for each of the two polar–orbiting satellites. These images can be combined to provide daily coverage of each polar region with horizontal resolution of 1.1 km at nadir. The spatial overlap of consecutive images allows for some tracking of cloud movement, although for a relatively short time period when compared to geostationary satellite data. AVHRR measurement characteristics, including the ability to measure with or without sunlight, offer unique advantages for PSC detection. *Garcia, et al.* [1995] and *Pagan* [1996] have shown that AVHRR measurements of 12 μm brightness temperature can be used to detect optically thick PSCs when underlying Earth surface temperatures are well above PSC temperatures. Most PSCs, however, are optically thin and occur over a variety of underlying surface conditions, and cannot be detected using a single AVHRR channel.

Cirrus and ice PSCs can have similar characteristics, so it is reasonable to expect that techniques established for cirrus characterization could be applied to PSC measurements. *Inoue* [1985, 1987] found that cirrus clouds can be identified over tropical oceans using the difference between channel 4 and 5 brightness temperatures (T_4 and T_5). This brightness temperature difference (BTD = $T_4 - T_5$) was then used by *Yamanouchi et al.* [1987] to detect thin cirrus over Antarctica. The radiative contrast between channels 4 and 5 has been investigated as a tool for inferring physical cloud properties such as temperature and particle effective radius [e.g., *Wu*, 1987; *Parol et al.*, 1991; *Lubin and Harper*, 1996]. Parol et al. concluded that while cloud effective radii cannot be accurately determined, that useful limits can be placed on its range. Lubin and Harper inferred the temperature, ice water path, and effective radius of Antarctic cirrus, and suggest that these properties can be determined with some certainty for conditions relevant to cirrus and PSCs.

For this work, the AVHRR channel 4 and 5 radiances were evaluated from a theoretical basis to understand the emission from clear and cloudy skies. Methods were developed for retrieving

cloud extinction optical depths, average temperature ($\bar{T}_c$), average effective radius ($\bar{r}_e$), and ice water path (IWP), from the channel 4 and 5 radiances. These retrievals were applied to AVHRR cloud measurements for comparison to values derived from radiosonde measurements and to measurements from the Polar Ozone and Aerosol Measurement (POAM) II instrument.

2. Radiative Transfer and Signal Simulation

The nadir emission from a column of atmosphere containing cloud, $L_m(\lambda)$, can be expressed in terms of net radiances (L) and transmissivities (τ)

$$L_m(\lambda) = \{ [L_E(\lambda) \tau_t(\lambda) + L_{At}(\lambda)] \tau_c(\lambda) + L_c(\lambda) \} \tau_u(\lambda) + L_{Au}(\lambda) \qquad (1)$$

where $L_E(\lambda)$ is due to the Earth's surface, $\tau_t(\lambda)$ and $L_{At}(\lambda)$ are due to clear air below the cloud layer, $\tau_c(\lambda)$ and $L_c(\lambda)$ are due to the cloud layer, and $\tau_u(\lambda)$ and $L_{Au}(\lambda)$ are due to clear air above the cloud. Each L and τ is an integral in height and wavelength, and the expanded relationship is tedious compared to (1). The terms in (1) are now explored.

2.1. Earth's Surface

Radiance emitted from the Earth's surface can be expressed in terms of the surface emissivity $\varepsilon_0(\lambda)$ and the blackbody radiance (L*) at surface temperature T_E, $L_E(\lambda) = L^*(T_E, \lambda) \varepsilon_0(\lambda)$. For typical surface cover underlying PSCs (sea water, snow, and ice), values of $\varepsilon_0(\lambda)$ are close to unity and are roughly constant in the 10 to 12 μm region (Table 1). Thus, the spectral content introduced to $L_m(\lambda)$ by $L_E(\lambda)$ is primarily that of the Planck function.

2.2 Clear Skies

Atmospheric absorption and emission were determined using rigorous line–by–line calculations [Gordley et al., 1994] for interfering gases in the channel 4 and 5 bandpasses. In order of radiative importance, the species considered were H_2O, CO_2, O_3, HNO_3, CCl_3F, and CCl_2F_2. Frequency integrals were convolved over the AVHRR spectral response functions to more accurately simulate an AVHRR measurement. The vertical integrals considered transfer from the Earth's surface to altitudes where gaseous contributions become negligible (about 50 km). Clear

sky radiances were simulated for conditions ranging from polar winter to tropical. For this purpose, vertical profiles of temperature, pressure, and gas mixing ratios were taken from climatologies. These calculations show that the atmospheric contribution is determined mainly by H_2O and CO_2 in the lower troposphere, and that transfer above the tropopause can be safely neglected (i.e., $\tau_u(\lambda) \simeq 1$ and $L_{Au}(\lambda) \simeq 0$). Thus, the clear sky emission, $L_{cs}(\lambda)$, is determined by the Earth's surface and radiative transfer in the troposphere, $L_{cs}(\lambda) = L_E(\lambda) \tau_t(\lambda) + L_{At}(\lambda)$.

The clear sky results allow some simplifications of (1) which lead to a more general expression for cloudy sky emission. $L_{cs}(\lambda)$ could be measured from clear sky adjacent to a cloud, allowing the cloudy sky radiance to be expressed in terms of two measurements and two cloud terms. In a more general sense, the radiance illuminating a cloud from beneath may be affected by uncharacterized cloud layers at lower altitude. Considering that this background radiance, $L_{bk}(\lambda)$, can be characterized by AVHRR measurements away from a cloud of interest, the cloudy sky emission (1) is reduced to

$$L_m(\lambda) = L_{bk}(\lambda) \tau_c(\lambda) + L_c(\lambda) \qquad (2)$$

where $L_{bk}(\lambda)$ can be from a clear background, $L_{bk}(\lambda)=L_{cs}(\lambda)$, or cloudy background. The form of (2) is similar to expressions derived by *Parol et al.* [1991] and *Lubin and Harper* [1996] for cloudy sky emission. Figure 1 depicts the concept of clear and cloudy sky signals adopted for this work. Potential limitations to this approach come quickly to mind. However, (2) eliminates the need to accurately characterize the Earth's surface and atmosphere for input to rigorous radiative transfer calculations.

The dependence of clear sky radiance on telescope scan angle should be understood since values of $L_{cs}(\lambda)$ and $L_m(\lambda)$ could be taken from measurements at different scan angles. Clear sky calculations for a range of scan angles considering tropical and polar conditions show that sensitivity to scan angle increases for optically thick (e.g., tropical) atmospheres. Transmissivity is noticeably reduced at large scan angles. However, emission increases in proportion to $\tau_t(\lambda)$ so that net radiance is relatively insensitive to scan angle (Figure 2).
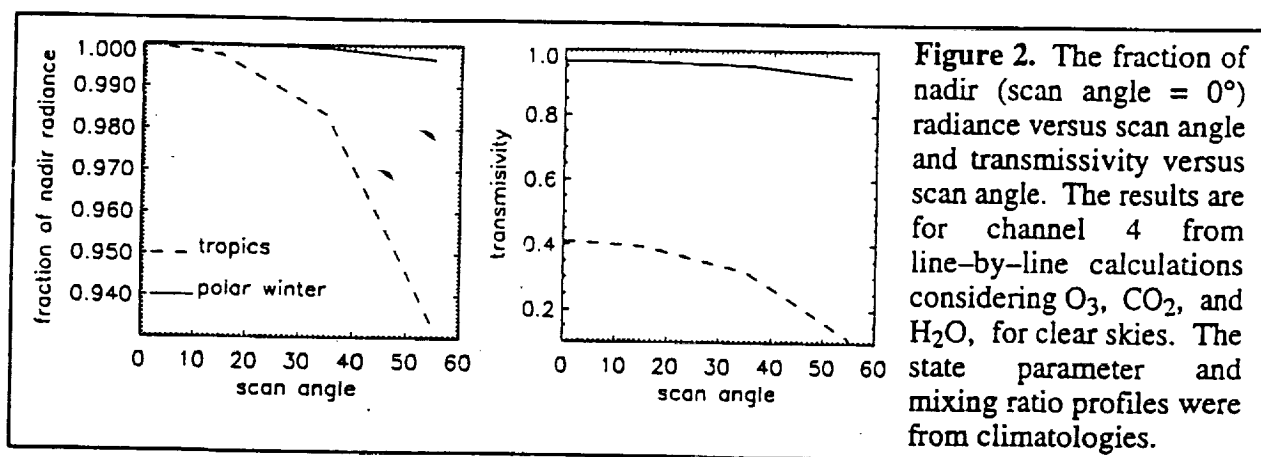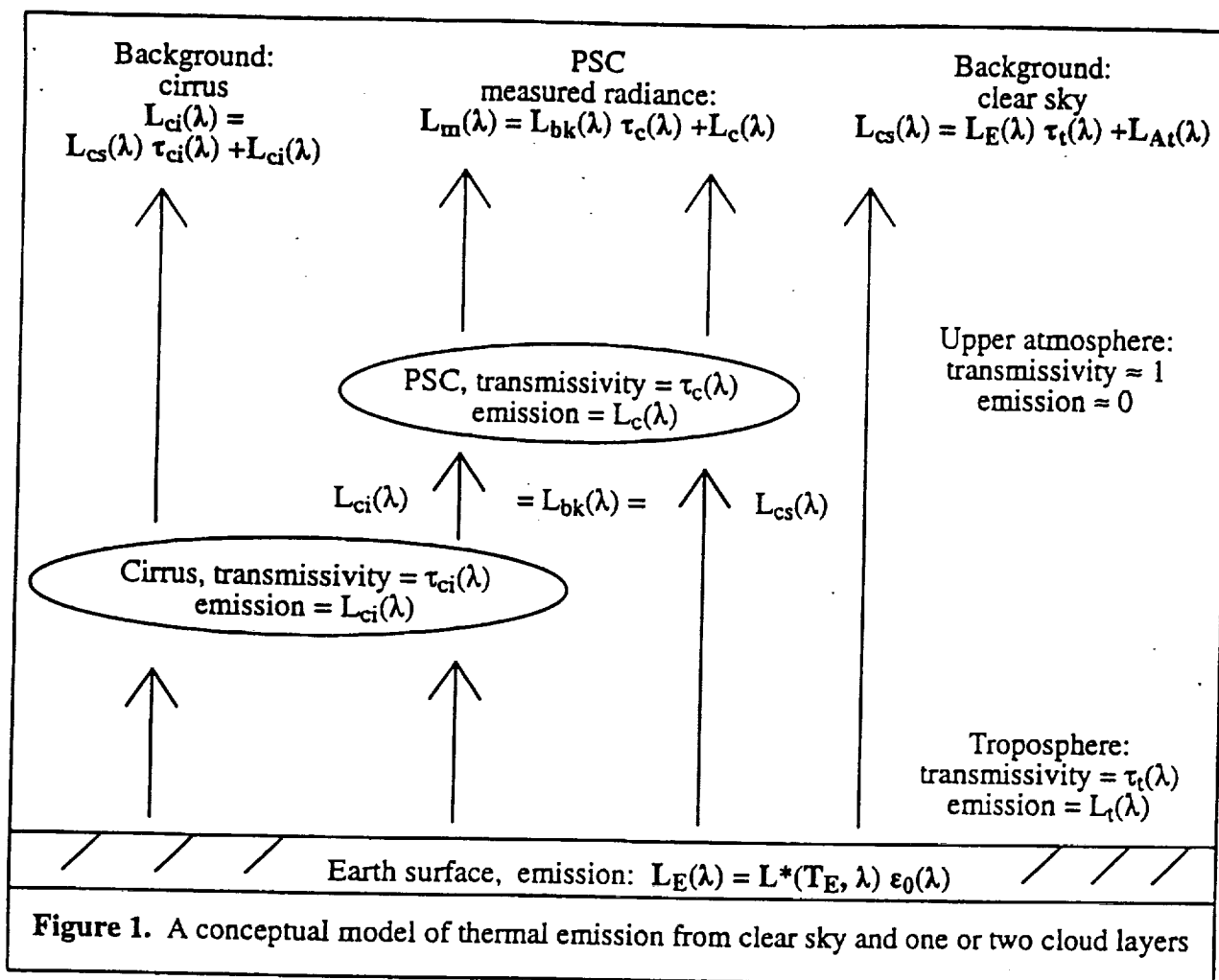
4

Figure 1. A conceptual model of thermal emission from clear sky and one or two cloud layers

Background:
cirrus
$$L_{ci}(\lambda) = L_{cs}(\lambda)\,\tau_{ci}(\lambda) + L_{ci}(\lambda)$$

PSC
measured radiance:
$$L_m(\lambda) = L_{bk}(\lambda)\,\tau_c(\lambda) + L_c(\lambda)$$

Background:
clear sky
$$L_{cs}(\lambda) = L_E(\lambda)\,\tau_t(\lambda) + L_{At}(\lambda)$$

Upper atmosphere:
transmissivity ≈ 1
emission ≈ 0

PSC, transmissivity $= \tau_c(\lambda)$
emission $= L_c(\lambda)$

$L_{ci}(\lambda)$ $= L_{bk}(\lambda) =$ $L_{cs}(\lambda)$

Cirrus, transmissivity $= \tau_{ci}(\lambda)$
emission $= L_{ci}(\lambda)$

Troposphere:
transmissivity $= \tau_t(\lambda)$
emission $= L_t(\lambda)$

Earth surface, emission: $L_E(\lambda) = L^*(T_E, \lambda)\,\varepsilon_0(\lambda)$

Figure 2. The fraction of nadir (scan angle $= 0°$) radiance versus scan angle and transmissivity versus scan angle. The results are for channel 4 from line–by–line calculations considering O_3, CO_2, and H_2O, for clear skies. The state parameter and mixing ratio profiles were from climatologies.

5

Table 1. Various Properties Relevant to AVHRR Channels 4 and 5.

Channel	Bandpass Wavelengths (μm): Lower Limit, Center, Upper Limit	Cloud Particle: Complex Refractive Index	Earth Surface: Emissivity
4	10.3, 10.8, 11.3[†]	ice: $1.09 + 0.18i$ (W) NAT: $1.63 + 0.13i$ (T) LTA: $1.58 + 0.24i$ (H)*	snow: 0.993 (M) sea ice: 0.985 (G) sea water: 0.991 (G)
5	11.5, 12.0, 12.5[†]	ice: $1.28 + 0.41i$ (W) NAT: $1.53 + 0.27i$ (T) LTA: $1.59 + 0.27i$ (H)*	snow: 0.972 (M) sea ice: 0.970 (G) sea water: 0.986 (G)

The information was taken from *Gao et al.* [1994] (G), MOSDIS UCSB Emissivity Library, www.icess.ucsb.edu (M), *Warren* [1984] (W), *Hervig et al.* [1997] (H), and *Toon et al.* [1994] (T). Refractive indices and emissivities are at the band center wavelengths.
*LTA at 192 K composed of 10 wt.% H_2SO_4 – 35 wt.% HNO_3.
[†]Values for the NOAA–12 sensor.

2.3. Cloud Optical Properties

The extinction coefficient (β_e) for a population of particles is calculated by integrating the extinction efficiency ($Q_e \equiv$ optical cross section / geometric cross section) over the size distribution:

$$\beta_e(\lambda) = \int_{r_1}^{r_2} \pi r^2 \, Q_e(r,\lambda,m) \, n(r) \, dr \qquad (3)$$

where m is particle refractive index (Table 1), n(r) is the particle size distribution, and r_1 and r_2 are the smallest and largest radii in the size distribution. The scattering coefficient (β_s) is calculated by substituting the scattering efficiency (Q_s) into (3), and the absorption coefficient (β_a) is the difference $\beta_e - \beta_s$.

The cloud particle size distribution can be described using a lognormal distribution for PSCs [*Deshler et al.*, 1994] or for cirrus [*Jensen et al.*, 1994]. While real cirrus or PSC size distributions can be quite different from lognormal, the lognormal form is useful for considering a broad range of conditions in modeling cloud radiative properties. The lognormal distribution is described by

$$n(r)dr = \sum_{i=1}^{k} N_i \frac{\exp\left[-\ln^2(r/\bar{r}_i) / (2\ln^2 w_i) \right]}{r \, (2\pi)^{(1/2)} \ln(w_i)} \qquad (4)$$
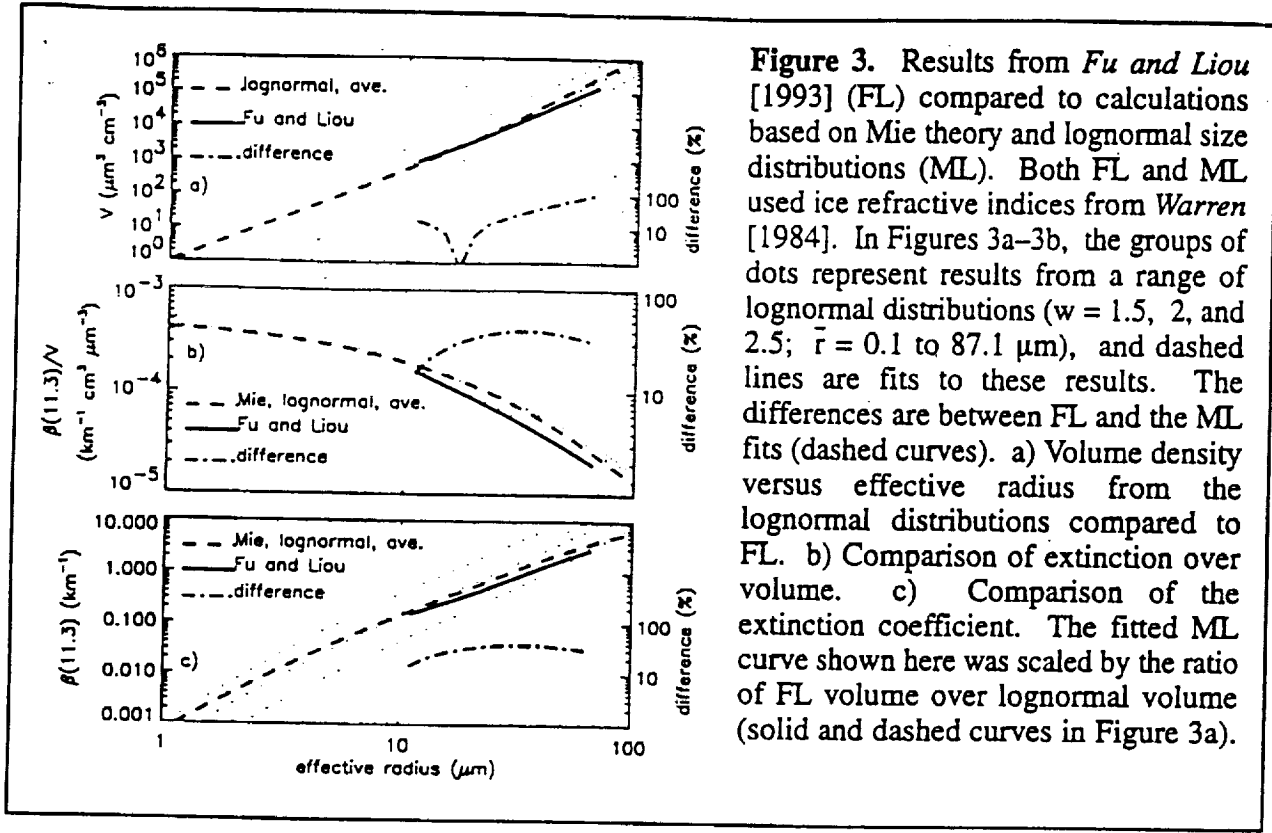
where n(r) is the differential concentration in the radius interval dr, k is the number of modes in the distribution, N_i is the number concentration, w_i is the distribution width, and $\bar{r}_i$ is the median radius,

for each of i modes. Cloud volume density (V, particle volume per unit volume of air) and effective radius (r_e, surface area weighted mean radius) can be derived from the size distribution. These important quantities are introduced here for convenience.

$$r_e = \bar{r} \exp[5 (\ln^2 w)/2] \tag{5}$$

$$V = N (4/3) \pi \bar{r}^3 \exp[8 (\ln^2 w)/2] \tag{6}$$

In this work, optical cross sections for (3) were determined using Mie theory, which explains the scattering and absorption by spheres. While cirrus and PSC particles are probably nonspherical, Mie theory can still provide reasonable estimates [e.g., *Ebert and Curry*, 1992]. To test this assumption, calculations based on Mie theory were compared to results from *Fu and Liou* [1993] (FL) who used ray tracing and spheroidal solutions to calculate extinction cross sections for randomly oriented hexagonal ice crystals. FL computed integral extinctions, $\beta_e(\lambda)$, for 11 measured size distributions and fit the ratio $\beta_e(\lambda)/V$ versus effective radius for numerous broad spectral bands across the visible and infrared. The bands used by FL did not match AVHRR channels 4 or 5, so one of their bands between 10.2 and 12.5 μm (central $\lambda = 11.3$ μm) was chosen for the comparisons. Using the Mie-lognormal model, $\beta_e(11.3)$ and V were calculated for a range of lognormal distributions. The resulting volumes encompass the FL results (Figure 3a), so it should be possible to mimic their size distributions by carefully selecting lognormal parameters. Because volume and extinction are roughly proportional, we expect the ratio $\beta_e(\lambda)/V$ to be somewhat independent of size distribution. To the extent that this is true, the comparison of $\beta_e(11.3)/V$ is a good measure of the differences between Mie extinction and the more rigorous calculations of FL (Figure 3b). The Mie extinctions were scaled by the ratio of volume from FL over the lognormal volume, to account for size distribution differences. The scaled Mie extinctions are 10 to 30% greater than FL (Figure 3c). However, it is evident in Figure 3c that the Mie-lognormal model could exactly reproduce FL by adjusting the choice of lognormal size distributions. Since FL considered only 11 size distributions, there is no reason to expect that their results are more versatile than results based on a large family of lognormal size distributions. Thus, this work proceeds using the readily available Mie-lognormal model.

Figure 3. Results from *Fu and Liou* [1993] (FL) compared to calculations based on Mie theory and lognormal size distributions (ML). Both FL and ML used ice refractive indices from *Warren* [1984]. In Figures 3a–3b, the groups of dots represent results from a range of lognormal distributions (w = 1.5, 2, and 2.5; r̄ = 0.1 to 87.1 μm), and dashed lines are fits to these results. The differences are between FL and the ML fits (dashed curves). a) Volume density versus effective radius from the lognormal distributions compared to FL. b) Comparison of extinction over volume. c) Comparison of the extinction coefficient. The fitted ML curve shown here was scaled by the ratio of FL volume over lognormal volume (solid and dashed curves in Figure 3a).

Cloud transmissivity is determined by radiative loss due to scattering and absorption (extinction) in the cloud layer,

$$\tau_c(\lambda) = \exp(-\beta_e(\lambda)\,\Delta z) \tag{7}$$

where Δz is geometric cloud thickness. Cloud emissivity is determined by a cloud's absorptive properties,

$$\varepsilon_c(\lambda) = 1 - \exp(-\beta_a(\lambda)\,\Delta z) \tag{8}$$

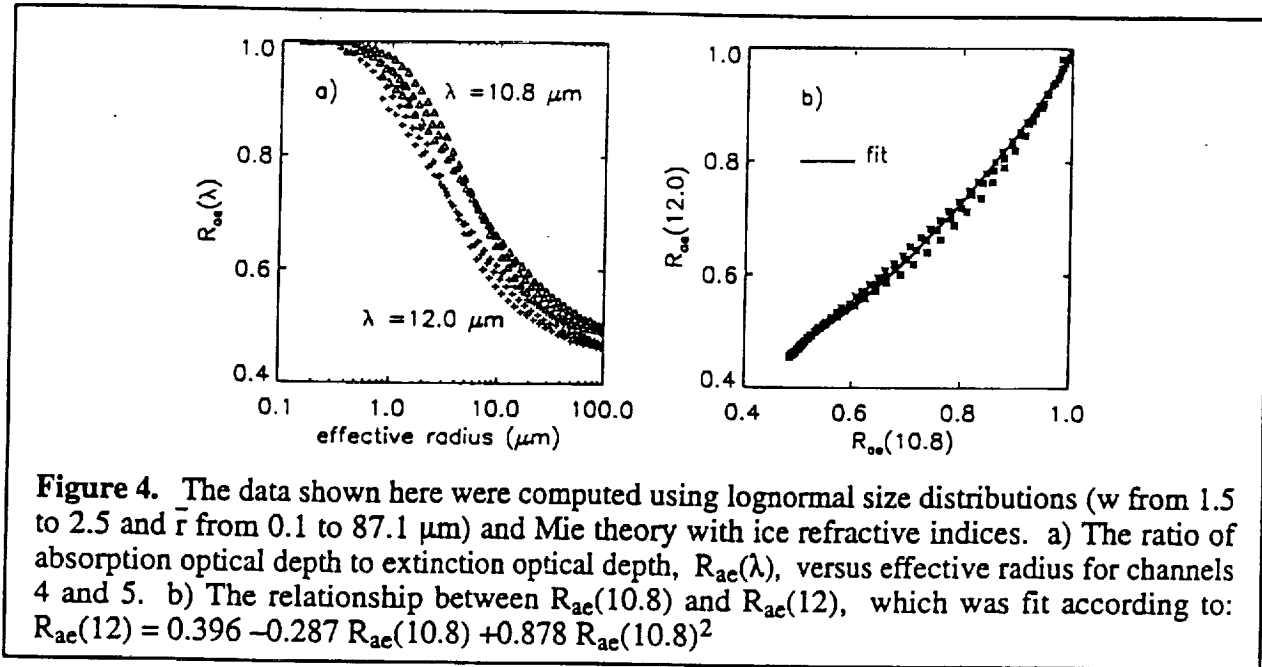and cloud radiance is determined by the cloud temperature ($\overline{T}_c$) and emissivity,

$$L_c(\lambda) = L^*(\overline{T}_c, \lambda)\,\varepsilon_c(\lambda) \tag{9}$$

where $L^*(\overline{T}_c, \lambda)$ is the blackbody radiance. Optical depth, $\sigma_e(\lambda) = \beta_e(\lambda)\Delta z$ or $\sigma_a(\lambda) = \beta_a(\lambda)\Delta z$, can be substituted into the above relationships. The cloudy sky emission (2) can be restated in terms of a single optical depth by defining the ratio $R_{ae}(\lambda) = \sigma_a(\lambda)/\sigma_e(\lambda)$ and substituting (7), (8), and (9).

$$L_m(\lambda) = L_{bk}(\lambda)\exp[-\sigma_e(\lambda)] + L^*(\overline{T}_c, \lambda)\{1 - \exp[-\sigma_e(\lambda)\,R_{ae}(\lambda)]\} \tag{10}$$

If $R_{ae}(\lambda)$ can be treated as constant, (10) defines a closed system, relating two measurements and two unknowns. Calculated values of $R_{ae}(\lambda)$ are bounded between 0.45 and 1.0 for ice refractive

8

indices and a range of size distributions representative of PSCs or cirrus (Figure 4a). It can also be shown that $R_{ae}(10.8)$ and $R_{ae}(12)$ are strongly correlated for ice indices and a wide range of size distributions (Figure 4b). While fixing $R_{ae}(\lambda)$ may or may not prove acceptable, its value is bounded and its importance therefore easily understood.

Figure 4. The data shown here were computed using lognormal size distributions (w from 1.5 to 2.5 and r̄ from 0.1 to 87.1 μm) and Mie theory with ice refractive indices. a) The ratio of absorption optical depth to extinction optical depth, $R_{ae}(\lambda)$, versus effective radius for channels 4 and 5. b) The relationship between $R_{ae}(10.8)$ and $R_{ae}(12)$, which was fit according to: $R_{ae}(12) = 0.396 - 0.287\ R_{ae}(10.8) + 0.878\ R_{ae}(10.8)^2$

The Mie–lognormal model was challenged to reproduce relationships between T_4 and BTD measured by AVHRR. For these simulations, it was necessary to vary optical depth to reproduce a measured range of brightness temperature. This can be accomplished by fixing number concentration and cloud thickness ($N\Delta z$) and varying r_e or by fixing r_e and varying $N\Delta z$ (equations 3, 4, and 10). While results from both approaches can be similar, fixing $N\Delta z$ and varying r_e usually gives the most convincing reproduction of the measured T_4 versus BTD. This is consistent with the understanding of crystal population growth, where particle concentration becomes stable shortly after cloud nucleation and particle size continues to increase as a cloud matures. While this generalization may not apply to a broad region of cloud, it is probably a good assumption for small cloud segments. In general the AVHRR measurements can be explained using the Mie–lognormal model, and an example comparison is offered in Figure 5.
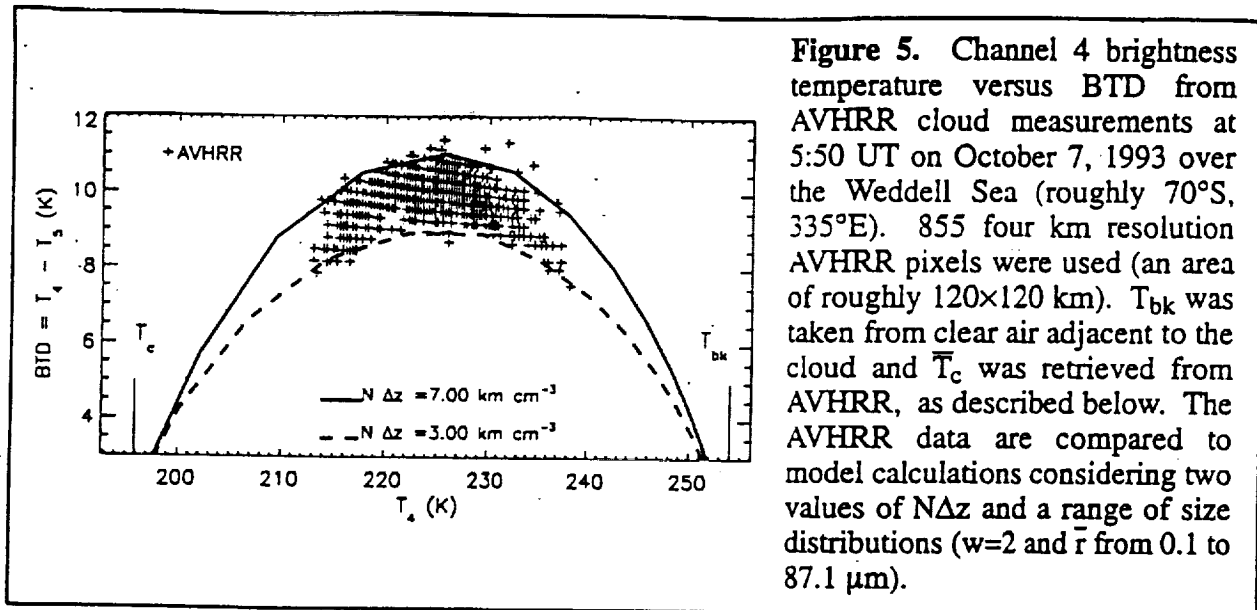
Figure 5. Channel 4 brightness temperature versus BTD from AVHRR cloud measurements at 5:50 UT on October 7, 1993 over the Weddell Sea (roughly 70°S, 335°E). 855 four km resolution AVHRR pixels were used (an area of roughly 120×120 km). T_{bk} was taken from clear air adjacent to the cloud and $\bar{T}_c$ was retrieved from AVHRR, as described below. The AVHRR data are compared to model calculations considering two values of NΔz and a range of size distributions (w=2 and $\bar{r}$ from 0.1 to 87.1 μm).

3. Predictions for PSCs at Equilibrium

It is useful to estimate optical depths and AVHRR signals expected for typical clouds. Given a pressure, temperature, and gas mixing ratios of H_2O (Q_w) and/or HNO_3 (Q_n), the volume densities of stratospheric ice, NAT, and LTA can be calculated from theory by assuming that vapor in excess of equilibrium condenses onto cloud particles [e.g., *Koop et al.*, 1997]. This treatment is valid because the stability of the stratosphere ensures that vapor loss to cloud growth is localized and therefore limited, on the time scale of a cooling event. This approach is invalid in the troposphere in principal because a cloud's vapor supply can be continuous. Infrared extinctions are strongly correlated to V, which allows the estimation of optical depths and therefore AVHRR signals. Figure 6a shows an example of the correlation between $\beta_e(\lambda)$ and V determined from theory. These data were fit according to

$$\log_{10}(\beta_e(\lambda)) = A + B \log_{10}(V) + C \log_{10}(V)^2 \qquad (11)$$

where A, B, and C are constants. Constants for (11) are given in Table 2 for ice and NAT and λ = 10.8 and 12.0 μm. In a different approach, the ratio $\beta_e(\lambda)/V$ can be determined versus effective radius (Figure 6b). Either approach is valid, and allows conversion from V to $\beta_e(\lambda)$.
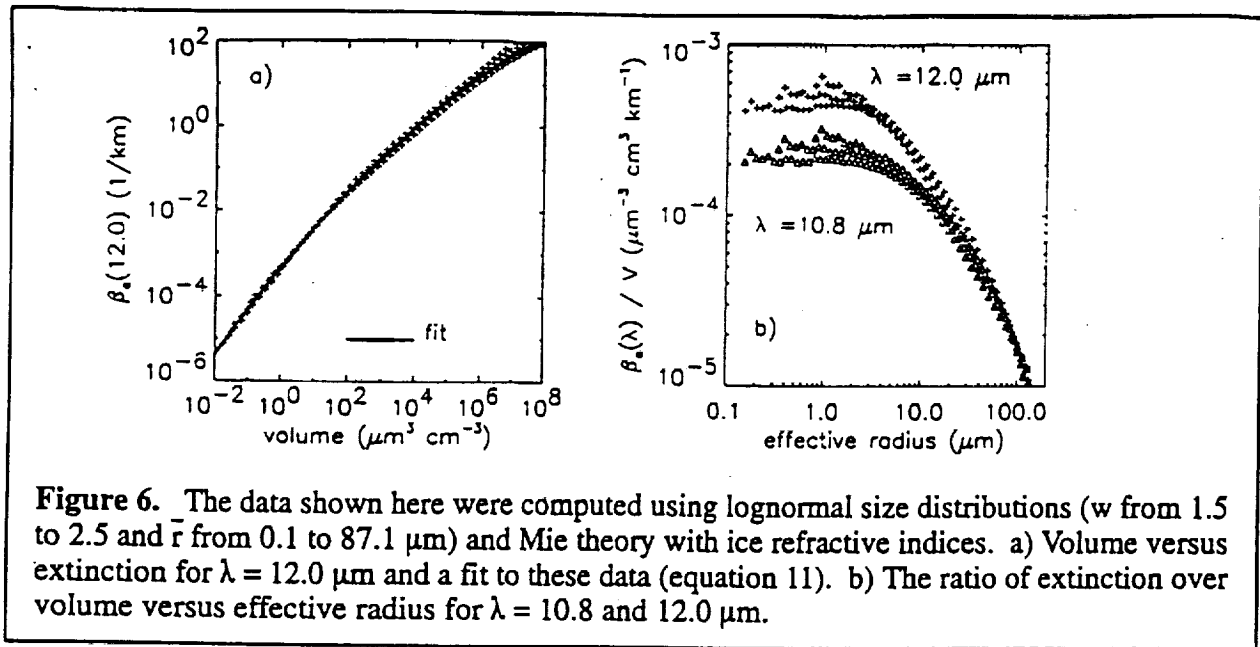
Figure 6. The data shown here were computed using lognormal size distributions (w from 1.5 to 2.5 and $\bar{r}$ from 0.1 to 87.1 μm) and Mie theory with ice refractive indices. a) Volume versus extinction for λ = 12.0 μm and a fit to these data (equation 11). b) The ratio of extinction over volume versus effective radius for λ = 10.8 and 12.0 μm.

Table 2. Constants for Equation 11.*

Wavelength (μm), particle type	A	B	C
10.8, NAT	−3.48	1.11	−0.054
10.8, ice	−3.56	1.00	−0.035
12.0, NAT	−3.40	1.04	−0.045
12.0, ice	−3.30	0.96	−0.035
*For $\beta_e(\lambda)$ in km^{-1} and V in μm^3 cm^{-3}.			

Volumes corresponding to a range of stratospheric temperatures and pressures were computed for upper limit mixing ratios of stratospheric H_2O (5 ppmv) [*Abbas et al.*, 1996] and HNO_3 (15 ppbv) [*Roche et al.*, 1993]. Peak NAT volumes (and therefore optical depths) are roughly three orders of magnitude less than peak ice volumes (Figure 7). This difference is due to the fixed stoichiometry of NAT so that HNO_3 becomes the limiting reagent for particle growth. Extinctions were determined from V, and optical depths were determined for fixed cloud thickness (Figure 7b). The optical depths were used with (10) to calculate the change in background sky brightness temperature ($L_{bk}(\lambda) = L^*(T_{bk}, \lambda)$) when clouds are introduced, $T_{bk} - T_m(\lambda)$, and associated cloudy air BTDs (BTD = $T_4 - T_5$) for assumed values of T_{bk} and $R_{ac}(\lambda)$. The thickest stratospheric NAT cloud ($\sigma_e(\lambda)$ less than about 10^{-2}) changes the background brightness temperature by less than 0.1 K and NAT PSCs can therefore be considered invisible to AVHRR. This conclusion holds for a
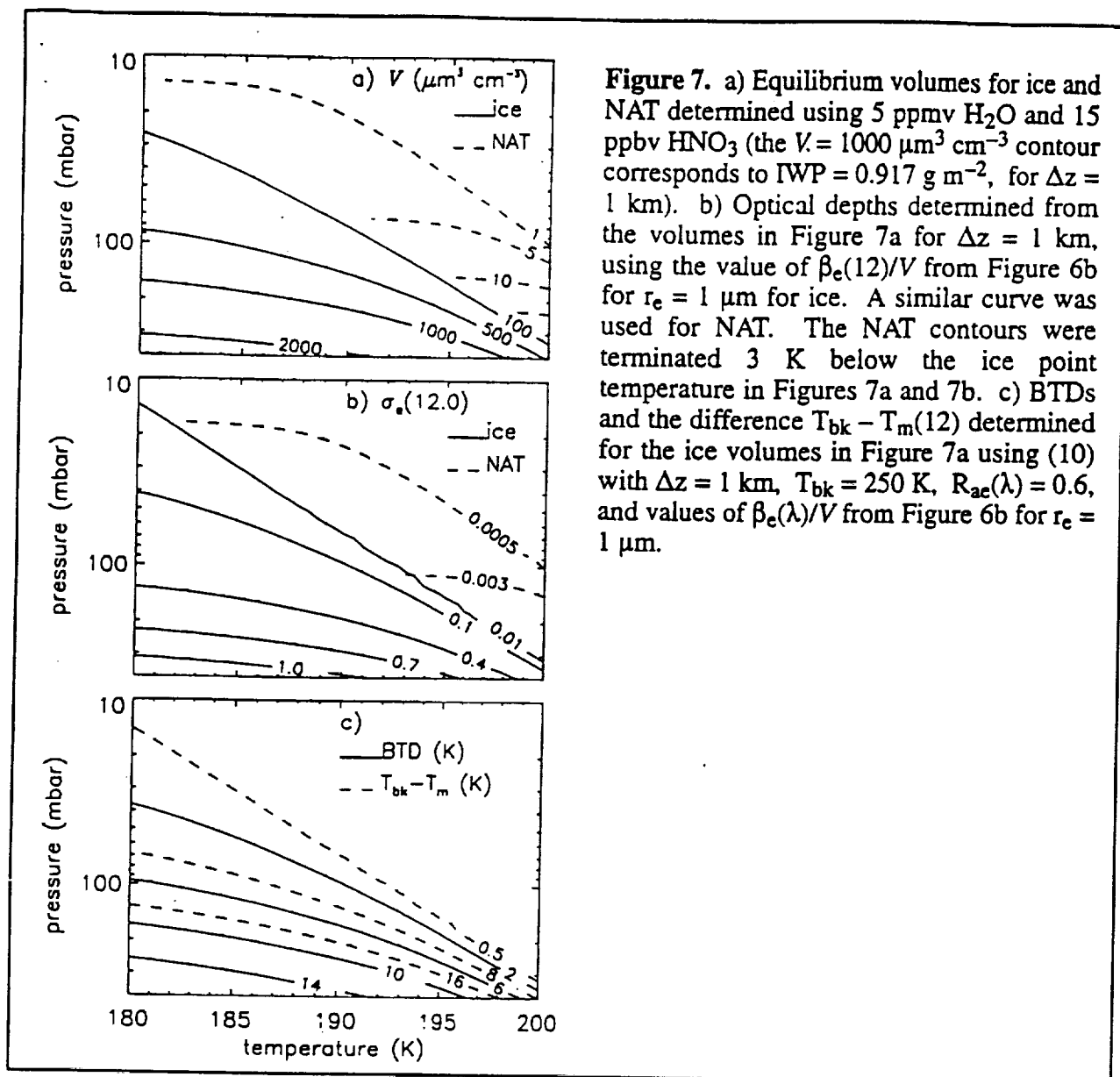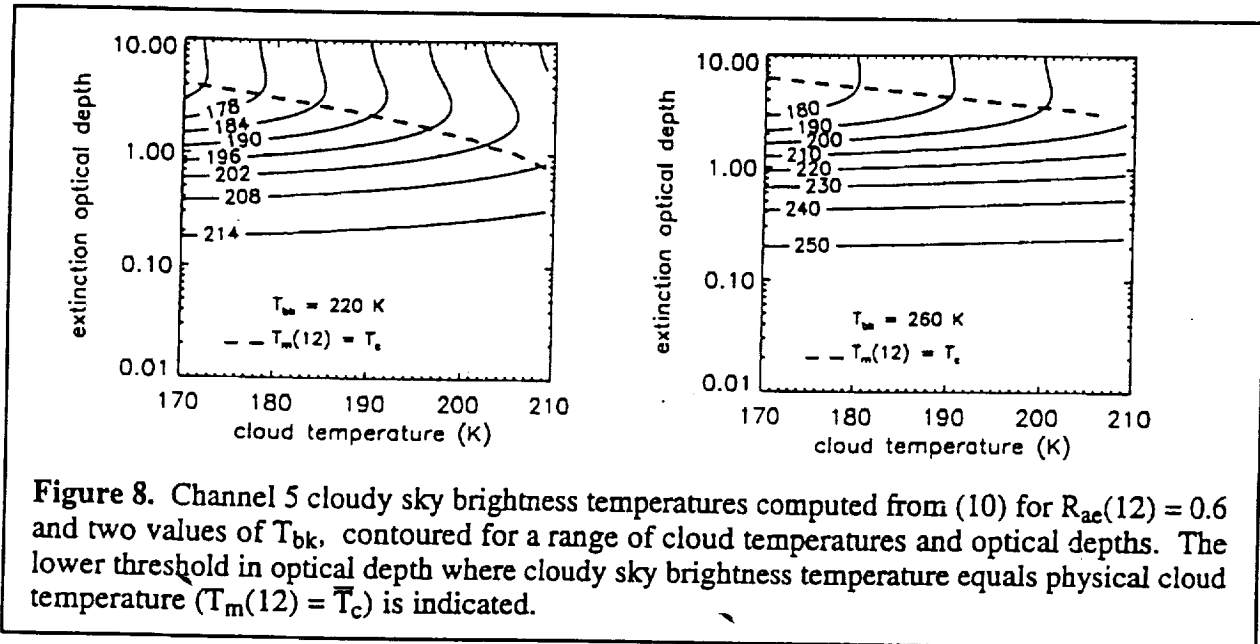
11

Figure 7. a) Equilibrium volumes for ice and NAT determined using 5 ppmv H_2O and 15 ppbv HNO_3 (the $V = 1000$ μm^3 cm^{-3} contour corresponds to IWP = 0.917 g m^{-2}, for $\Delta z = 1$ km). b) Optical depths determined from the volumes in Figure 7a for $\Delta z = 1$ km, using the value of $\beta_e(12)/V$ from Figure 6b for $r_e = 1$ μm for ice. A similar curve was used for NAT. The NAT contours were terminated 3 K below the ice point temperature in Figures 7a and 7b. c) BTDs and the difference $T_{bk} - T_m(12)$ determined for the ice volumes in Figure 7a using (10) with $\Delta z = 1$ km, $T_{bk} = 250$ K, $R_{ae}(\lambda) = 0.6$, and values of $\beta_e(\lambda)/V$ from Figure 6b for $r_e = 1$ μm.

broad range of conditions ($R_{ae}(\lambda)$, T_{bk}, and $\overline{T}_c$), and the same conclusion is drawn for PSCs composed of LTA. Considering that the stratospheric conditions in Figure 7 are generous in terms of pressure and mixing ratio (in reality HNO_3 disappears near the tropopause), this conclusion is well founded and the remainder of this study proceeds without consideration of NAT or LTA. The thickest ice PSCs change T_{bk} by up to 16 K and produce BTDs of up to 14 K, for the scenario presented in Figure 7c. $T_{bk} - T_m$ is less sensitive to the shape of the size distribution than BTD, and the estimates of BTD in Figure 7c can change notably for using different size distributions, due to the dependence of $R_{ae}(\lambda)$ on particle size (Figure 4a). Calculations considering tropospheric

conditions produce a broad range of optical depths and BTDs, which include stratospheric values. Thus, a threshold optical depth could be determined which precludes a cloud from being stratospheric. However, a threshold which precludes a cloud from being tropospheric is more elusive.

It is useful to consider the relationship between cloud optical depth, cloud temperature, and brightness temperature. Figure 8 shows example calculations for a single cloud layer in an otherwise clear atmosphere. In order for a cloud to radiate at its physical temperature ($T_m(\lambda) = \overline{T}_c$), its optical depth must be greater than about one. Optical depths which produce $T_m(\lambda) = \overline{T}_c$ decrease with decreasing T_{bk} (or increasing $\overline{T}_c$), although they are often near the upper limit for ice PSC optical depth (Figure 7b).

Figure 8. Channel 5 cloudy sky brightness temperatures computed from (10) for $R_{ae}(12) = 0.6$ and two values of T_{bk}, contoured for a range of cloud temperatures and optical depths. The lower threshold in optical depth where cloudy sky brightness temperature equals physical cloud temperature ($T_m(12) = \overline{T}_c$) is indicated.
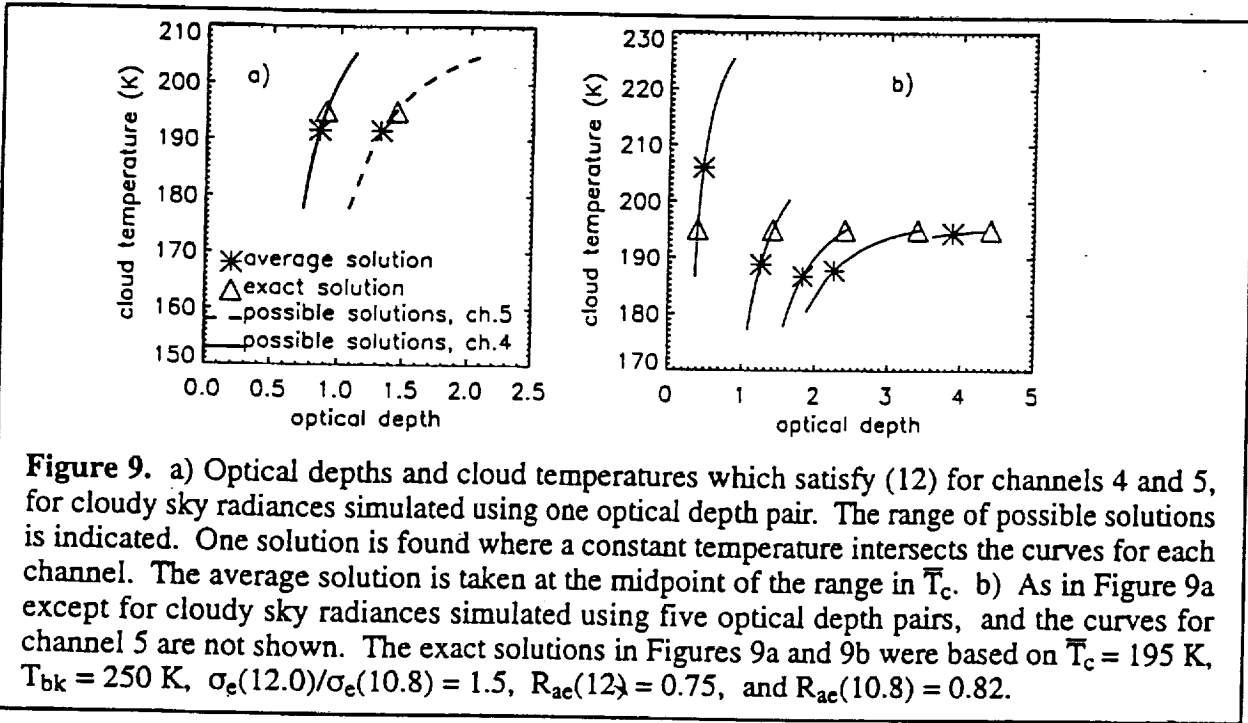
4. Cloud Property Retrievals

4.1. Cloud Temperature and Optical Depth

Given cloudy and background sky measurements from both channels, it is possible to retrieve $\overline{T}_c$, $\sigma_e(10.8)$, and $\sigma_e(12.0)$ simultaneously. This is accomplished by solving (10) for the blackbody cloud radiance $L^*(\overline{T}_c, \lambda)$,
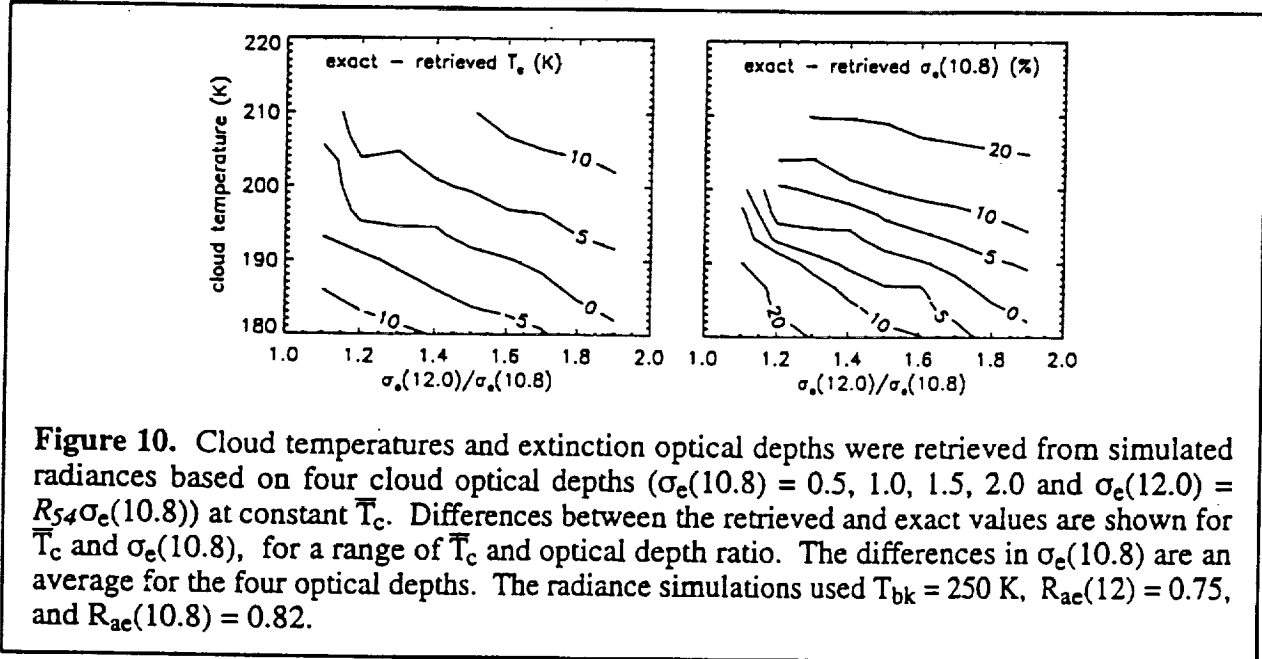
$$L \cdot (T_c, \lambda) = \frac{L_m(\lambda) - L_{bk}(\lambda) \, exp[-\sigma_e(\lambda)]}{1 - exp[-\sigma_e(\lambda) R_{ae}(\lambda)]} \tag{12}$$

and finding $\overline{T}_c$ through the Planck function. Cloud temperatures can be determined from (12) for a range of synthetic optical depths and fixed $R_{ae}(\lambda)$. This step is performed for each channel and a solution is taken where both channels yield the same cloud temperature. Solutions are not unique, yet the range of possible solutions usually contains the exact solution. It is difficult, however, to discern the correct solution from this family of possibilities. One approach is to find the average temperature, and use the corresponding optical depths. The retrieval approach is demonstrated in Figure 9a, where cloudy sky radiances were simulated for known conditions and (12) was solved

Figure 9. a) Optical depths and cloud temperatures which satisfy (12) for channels 4 and 5, for cloudy sky radiances simulated using one optical depth pair. The range of possible solutions is indicated. One solution is found where a constant temperature intersects the curves for each channel. The average solution is taken at the midpoint of the range in $\overline{T}_c$. b) As in Figure 9a except for cloudy sky radiances simulated using five optical depth pairs, and the curves for channel 5 are not shown. The exact solutions in Figures 9a and 9b were based on $\overline{T}_c = 195$ K, $T_{bk} = 250$ K, $\sigma_e(12.0)/\sigma_e(10.8) = 1.5$, $R_{ae}(12) = 0.75$, and $R_{ae}(10.8) = 0.82$.

for both channels to determine $\overline{T}_c$, $\sigma_e(10.8)$, and $\sigma_e(12.0)$. While an average solution can be a good approximation in some cases, it can be biased by over 10 K in others. The assumption is now made that horizontal variations in cloud radiance over small distances are due to changes in optical depth, while temperature remains fairly constant. This is an important characteristic because for cloud radiances corresponding to a range of σ_e at constant $\overline{T}_c$ the families of solutions tend to overlap around the exact value of $\overline{T}_c$. This behavior is demonstrated in Figure 9b, where the potential improvements for considering a range of optical depth are apparent. The errors for retrievals based

on a single measurement are greatest at low to intermediate optical depths, while $\overline{T}_c$ can be accurately determined for optically thick clouds (Figure 9b). Uncertainties in retrieved $\overline{T}_c$ and σ_e were determined for a range of $\overline{T}_c$ and optical depth ratio, $R_{54} = \sigma_e(12.0) / \sigma_e(10.8)$. In general, R_{54} ranges from two for $r_e = 0.1$ μm to unity for $r_e = 100$ μm. The fundamental uncertainties in retrieved $\overline{T}_c$ and σ_e are systematic (Figure 10) for a chosen scenario of cloud properties. Of course, since the cloud properties are unknown for a real measurement, the uncertainties will take on a more random nature.

Figure 10. Cloud temperatures and extinction optical depths were retrieved from simulated radiances based on four cloud optical depths ($\sigma_e(10.8) = 0.5$, 1.0, 1.5, 2.0 and $\sigma_e(12.0) = R_{54}\sigma_e(10.8)$) at constant $\overline{T}_c$. Differences between the retrieved and exact values are shown for $\overline{T}_c$ and $\sigma_e(10.8)$, for a range of $\overline{T}_c$ and optical depth ratio. The differences in $\sigma_e(10.8)$ are an average for the four optical depths. The radiance simulations used $T_{bk} = 250$ K, $R_{ae}(12) = 0.75$, and $R_{ae}(10.8) = 0.82$.
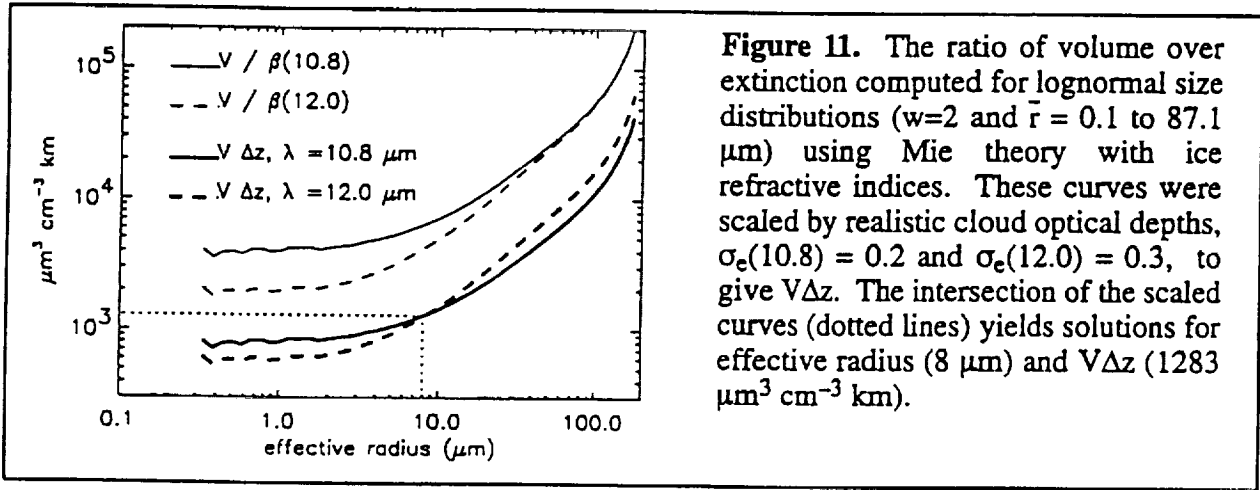
4.2. Effective Radius and Ice Water Path

As illustrated in Figure 6, the ratio $\beta_e(\lambda)/V$ can be a unique function in effective radius. Furthermore, it can be shown that the two functions, $f(r_e, 10.8) = V/\beta_e(10.8)$ and $f(r_e, 12.0) = V/\beta_e(12.0)$, are monotonic and non–intersecting for roughly $2 < r_e < 100$ μm. Curves for $f(r_e, \lambda)$ can be generated using a broad range of size distributions and thus r_e. Scaling $f(r_e, \lambda)$ by a measured optical depth yields a relationship between and r_e and $V\Delta z$, $f_s(r_e, \lambda) = f(r_e, \lambda)\sigma_e(\lambda) = V\Delta z$. Because the atmospheric values of $V\Delta z$ and r_e will be unique for a given measurement, a broad range of size distributions can be searched for one that yields the same r_e and $V\Delta z$ from both channels, $f_s(r_e, 10.8) = f_s(r_e, 12.0)$,

$$\frac{V(r_e)\,\Delta z}{\beta_e(12.0, r_e)\,\Delta z}\,\sigma_e(12.0) = \frac{V(r_e)\,\Delta z}{\beta_e(10.8, r_e)\,\Delta z}\,\sigma_e(10.8) \qquad (13)$$

where the optical depths are from AVHRR. For illustration, $f(r_e, 10.8)$ and $f(r_e, 12.0)$ were calculated using Mie theory with lognormal size distributions. These curves were scaled by realistic channel 4 and 5 optical depths, and solutions for r_e and $V\Delta z$ are found at their intersection (Figure 11). The ice water path is easily calculated, $IWP = V\Delta z\,\varrho_i$. While size distributions that satisfy (13) can vary, the integral quantities tend to fall in a narrower range. Never the less, the curves describing $f_s(r_e, \lambda)$ tend to have steep intersections, so that solutions become highly sensitive to errors in optical depth.

Figure 11. The ratio of volume over extinction computed for lognormal size distributions (w=2 and $\bar{r}$ = 0.1 to 87.1 μm) using Mie theory with ice refractive indices. These curves were scaled by realistic cloud optical depths, $\sigma_e(10.8) = 0.2$ and $\sigma_e(12.0) = 0.3$, to give $V\Delta z$. The intersection of the scaled curves (dotted lines) yields solutions for effective radius (8 μm) and $V\Delta z$ (1283 $\mu m^3\,cm^{-3}$ km).

To arrive at the curves in Figure 11, the size distribution width was fixed and the median radius was varied. This scenario yields one solution. However, a variety of realistic scenarios can yield solutions. Sensitivity of r_e and $V\Delta z$ to the choice of size distribution scenario was evaluated by generating optical depths and corresponding values of r_e and $V\Delta z$ for a broad range of size distributions. These synthetic optical depths were then used with the curves in Figure 11 to retrieve r_e and $V\Delta z$, for comparison to the known values. For each value of r_e, the uncertainty analysis used a Monte Carlo approach considering randomly chosen distributions which satisfy (5). Random and systematic variability about a known solution were then calculated from this sample set, to determine the effects of searching a limited set of size distributions for a solution. The effects of 10% random errors in the retrieved optical depths were then added to the size distribution errors for these calculations. Random uncertainties in r_e due to uncertainties in the size distribution are less

than 30% for the range of r_e considered (Figure 12a). When errors in retrieved optical depth are added, random uncertainties in r_e increase to over 50%, and significant retrieval bias appears for $r_e < 3$ μm and $r_e > 30$ μm (Figure 12a). Uncertainties in r_e and $V\Delta z$ due to size distribution and optical depth errors are summarized in Figure 12b, showing nearly 100% uncertainty in both for some size regimes. While r_e and $V\Delta z$ cannot be accurately determined, limits can be placed on their possible range, as concluded by *Parol et al.* [1991]. These large uncertainties may be tolerable for some applications, and averaging retrieved values over many pixels may provide some reduction in uncertainty.
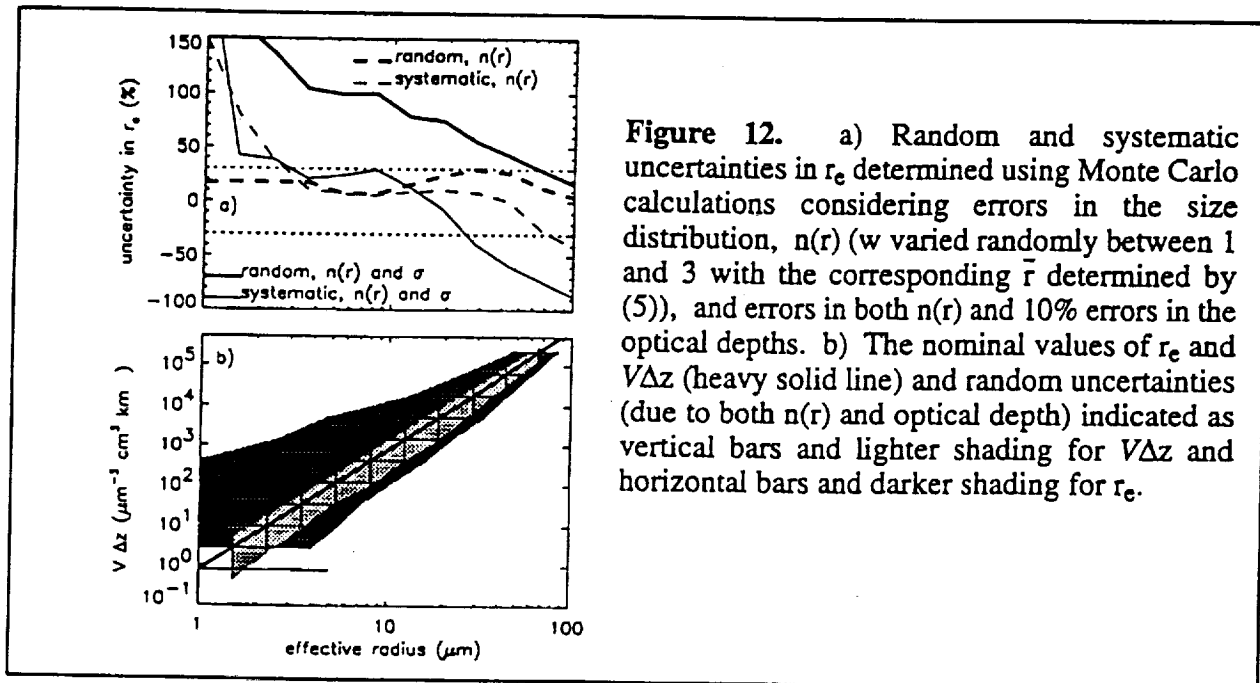
Figure 12. a) Random and systematic uncertainties in r_e determined using Monte Carlo calculations considering errors in the size distribution, n(r) (w varied randomly between 1 and 3 with the corresponding $\bar{r}$ determined by (5)), and errors in both n(r) and 10% errors in the optical depths. b) The nominal values of r_e and $V\Delta z$ (heavy solid line) and random uncertainties (due to both n(r) and optical depth) indicated as vertical bars and lighter shading for $V\Delta z$ and horizontal bars and darker shading for r_e.

5. Results Using AVHRR

Cloud properties retrieved from AVHRR were compared to values derived using measurements from radiosondes and from POAM II. For this purpose, raw AVHRR data were calibrated and geo-registered at 4km horizontal resolution [e.g., *Lubin and Harper*, 1996].

As previously discussed, equilibrium theory allows stratospheric ice clouds to be characterized from temperature, pressure, and water vapor mixing ratio (Q_w). While radiosondes provide reliable temperature and pressure measurements, they cannot measure Q_w in the

stratosphere. Stratospheric water vapor, however, is fairly uniform and has a well known upper limit near ~5 ppmv [e.g., *Abbas et al.*, 1996]. Assuming constant Q_w, stratospheric radiosonde profiles were used to calculate V and $\beta_e(\lambda)$ (as in Figure 7), which were integrated vertically to yield IWP and $\sigma_e(\lambda)$. $\overline{T}_c$ was then computed from a volume weighted mean for all cloud layers. The abundance of radiosonde measurements and the straightforward analysis provide a useful approach for validating retrievals of $\overline{T}_c$, $\sigma_e(\lambda)$, and IWP from AVHRR ice PSC measurements. An example radiosonde analysis is shown in Figure 13, where two values of constant Q_w were considered. In this example, changing Q_w from 5 to 3 ppmv reduces $\sigma_e(\lambda)$ and IWP by a factor of four, while $\overline{T}_c$ is relatively unaffected. Despite sensitivity to Q_w, radiosonde IWP and $\sigma_e(\lambda)$ provide reliable upper limits, and therefore useful validation data.
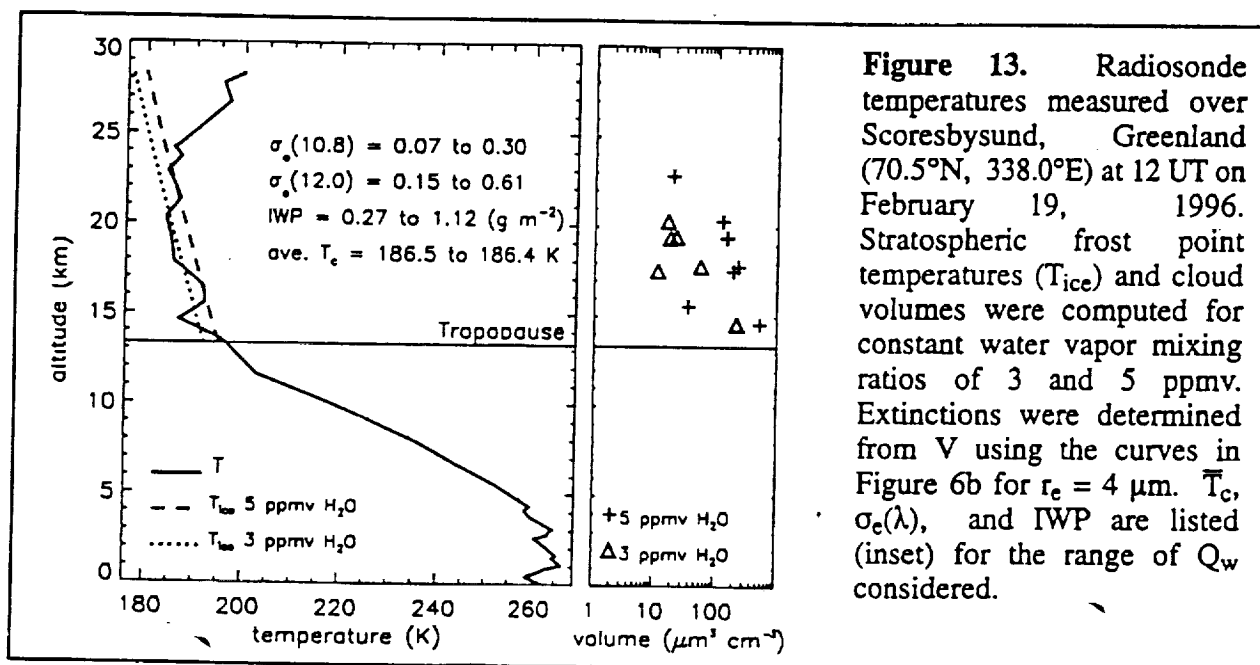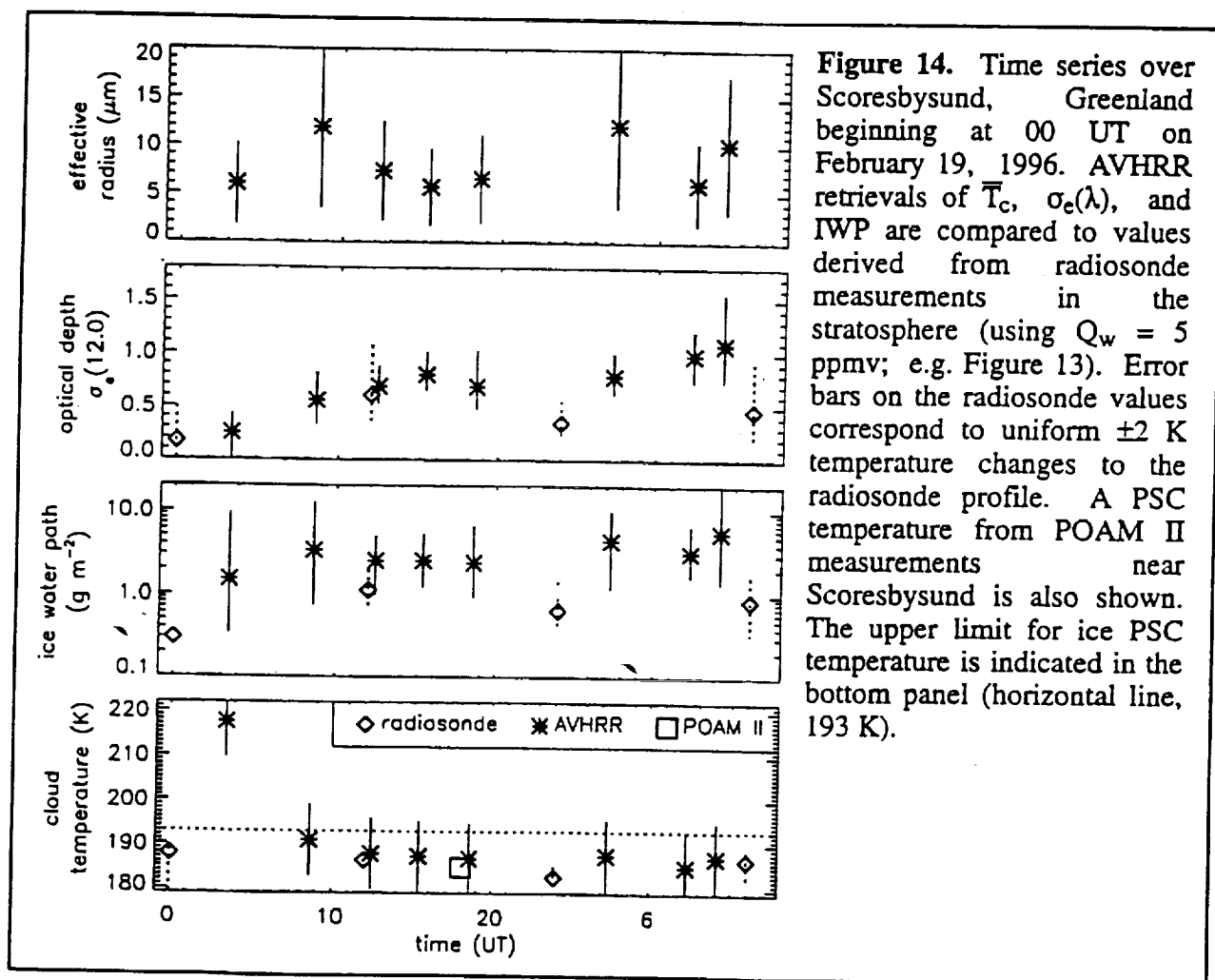

Figure 13. Radiosonde temperatures measured over Scoresbysund, Greenland (70.5°N, 338.0°E) at 12 UT on February 19, 1996. Stratospheric frost point temperatures (T_{ice}) and cloud volumes were computed for constant water vapor mixing ratios of 3 and 5 ppmv. Extinctions were determined from V using the curves in Figure 6b for $r_e = 4$ μm. $\overline{T}_c$, $\sigma_e(\lambda)$, and IWP are listed (inset) for the range of Q_w considered.

AVHRR cloud temperatures were also compared to solar occultation measurements from POAM II [*Randall et al.*, 1996]. Ice PSCs are identified in POAM II aerosol extinction profiles when the signal saturates in the stratosphere, temperatures are below T_{ice}, and the termination altitude is above the coldest layer in the profile [*Fromm et al.*, 1999]. When these criteria are met, PSC tops are estimated to occur from 1 to 2 km below the profile termination altitude, and PSC temperature can be estimated from the corresponding temperature profile.
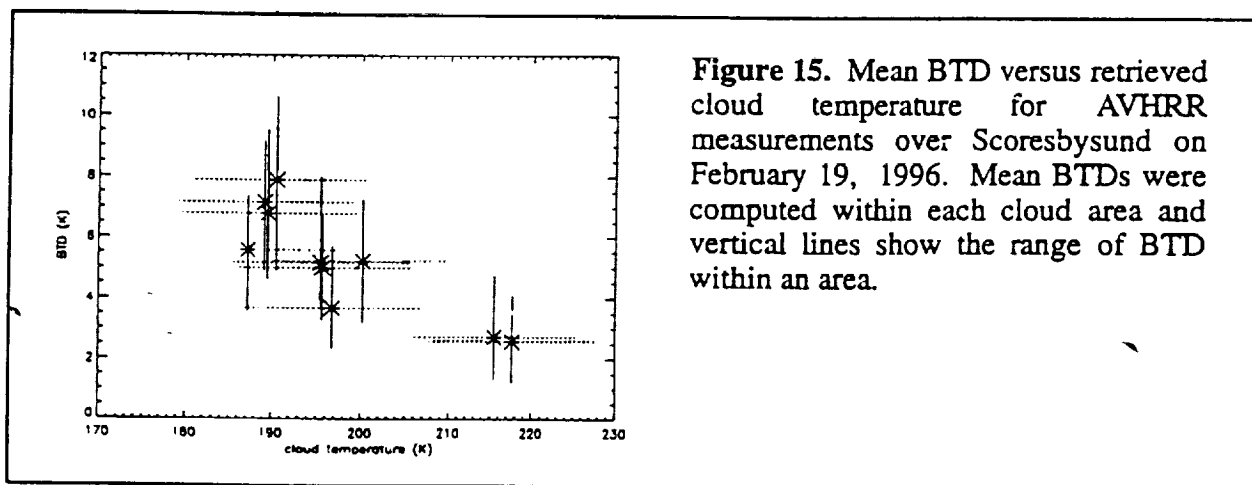
A case study of clouds over Scoresbysund, Greenland beginning on February 19, 1996 was used to test the AVHRR retrievals by comparing them with radiosondes and POAM II. AVHRR imagery on this day show clouds with brightness temperatures (T_5) between 189 and 200 K over much of Greenland. A cloudy area within roughly 200 km of Scoresbysund was selected from each AVHRR image for the cloud property retrievals. Each AVHRR cloud area was comprised of about 100 to 300 pixels (an area of roughly 1600 to 4900 km^2), and the cloud temperature retrievals used all pixels in an area to ensure variability in optical depth for reduced retrieval errors (e.g. Figure 9b). Values of r_e, $\sigma_e(\lambda)$, and IWP are presented as averages of all retrievals in a cloud area. Time series from AVHRR and the radiosondes are compared in Figure 14. These time series depict the passage

Figure 14. Time series over Scoresbysund, Greenland beginning at 00 UT on February 19, 1996. AVHRR retrievals of $\overline{T}_c$, $\sigma_e(\lambda)$, and IWP are compared to values derived from radiosonde measurements in the stratosphere (using $Q_w = 5$ ppmv; e.g. Figure 13). Error bars on the radiosonde values correspond to uniform ±2 K temperature changes to the radiosonde profile. A PSC temperature from POAM II measurements near Scoresbysund is also shown. The upper limit for ice PSC temperature is indicated in the bottom panel (horizontal line, 193 K).

of various PSCs and cirrus over Scoresbysund, rather than the evolution of a single stationary cloud. The AVHRR cloud temperature at 3 UT on the 19th is too warm to be stratospheric, even when

considering a possible 10 K overestimation at low optical depth (e.g., Figure 9). The other AVHRR cloud temperatures are consistent with PSCs, and are in good agreement with coincident POAM II and radiosonde data. The AVHRR retrievals of r_e, $\sigma_e(\lambda)$, and IWP are consistent with PSC conditions, yet they do not exclude the possibility of cirrus. Although AVHRR $\sigma_e(\lambda)$ and IWP retrievals tend to be larger than the radiosonde values, the two data sets agree within the mutual error limits.

Lubin and Harper [1996] suggested that BTDs greater than about 5 K may be characteristic of ice PSCs. Their idea was tested in this work using the relationship between measured BTD and retrieved cloud temperature from the AVHRR measurements over Scoresbysund. For these measurements, stratospheric frost point temperatures (T_{ice}) were always less than about 193 K (e.g. Figure 13). Thus the Scoresbysund AVHRR data suggest that ice PSCs are associated with BTDs greater than about 5 K (Figure 15), consistent with the suggestion of Lubin and Harper. The use of BTD as a PSC identifier may involve more than simply defining a threshold value, and this idea is currently the subject of rigorous evaluations based on model calculations and observations.

Figure 15. Mean BTD versus retrieved cloud temperature for AVHRR measurements over Scoresbysund on February 19, 1996. Mean BTDs were computed within each cloud area and vertical lines show the range of BTD within an area.

6. Summary

AVHRR channel 4 and 5 radiances from clear and cloudy skies were evaluated from a theoretical basis and techniques were presented for inferring cloud optical depth at $\lambda = 10.8$ and 12 μm, average temperature, average effective radius, and ice water path, for ice PSCs or cirrus. The

cloud optical depth and temperature retrievals assume that upwelling radiation beneath a cloud layer can be characterized from adjacent measurements, and that radiance variations across small cloud segments are due to variations in optical depth at constant average cloud temperature. The retrieval of ice water path and average effective radius requires signal simulations, which were based on Mie theory and lognormal size distributions. While the retrieval assumptions and signal simulations can have obvious limitations, they are justifiable for a useful portion of the AVHRR data set. Initial assessments show that AVHRR cloudy sky measurements can be explained in terms of the Mie–lognormal model. Additionally, cloud temperatures, ice water paths, and optical depths retrieved from AVHRR are in good agreement with values derived from coincident radiosonde measurements.

While large values of optical depth, effective radius, and ice water path can preclude the possibility of PSCs, small values do not bar the possibility of cirrus. Thus retrieved cloud temperatures should provide the most useful information for separating PSCs and cirrus in AVHRR data. The retrieval methods described in this paper require a considerable amount of image interpretation to determine an accurate underlying background temperature as input to the calculations. While this approach is useful for specific case studies, in its current form it would be difficult to employ on the entire AVHRR data set. There is compelling evidence, however, that BTDs could be a straightforward PSC identifier which can be easily applied to the extensive AVHRR data set, allowing the development of first–ever PSC climatologies in both hemispheres.

References

Abbas, M. M., et al., Seasonal variations of water vapor in the lower stratosphere inferred from ATMOS/ATLAS–3 measurements of H_2O and CH_4, *Geophys. Res. Lett.*, 23, 2401–2404, 1996.

Borrmann, S., S. Solomon, J. E. Dye, B. Luo, The potential of cirrus clouds for heterogeneous chlorine activation, *Geophys. Res. Letters*, 23, 2133–2136, 1996.

Carslaw, K. S., B. P. Luo, S. L. Clegg, Th. Peter, P. Brimblecombe, and P. J. Crutzen, Stratospheric aerosol growth and gas phase denitrification from nitric acid and water uptake by liquid particles, *Geophys. Res. Lett.*, 21, 2479–2482, 1994.

Deshler, T., B. J. Johnson, W. R. Rozier, Changes in the character of polar stratospheric clouds over Antarctica in 1992 due to the Pinatubo volcanic aerosol, *Geophys. Res. Letters*, 21, 273–276, 1994.

Ebert, E. E., and J. A. Curry, A parameterization of ice cloud optical properties for climate models, *J. Geophys. Res.*, 97, 3831–3836, 1992.

Fromm, M. D., R. M. Bevilacqua, J. Hornstein, E. Shettle, K. Hoppel, and J. Lumpe, An analysis of POAM II Arctic polar stratospheric cloud observations, 1993–1996, *J. Geophys. Res.*, in press, 1999.

Fu, Q., and K. N. Liou, Parameterization of the radiative properties of Cirrus Clouds, *J. Atm. Sci.*, 50, 2008–2025, 1993.

Gao, B., and W. J. Wiscombe, Surface–induced brightness temperature variations and their effects on detecting thin cirrus clouds using IR emission channels in the 8–12 μm region, *J. Appl. Meteor.*, 33, 568–570, 1994.

Garcia, O., K. Pagan, P. Foschi, S. Gaines and R. S. Hipskind, Detection of polar stratospheric clouds over Antarctica using AVHRR images obtained at Palmer Station during August 1992. *Polar Record*, 31, 211–226, 1995.

Gordley, L. L., et al., LINEPAK: Algorithms for modeling spectral transmittance and radiance, *J. Quant. Spectrosc. Radiat. Transfer*, 52, 563–580, 1994.

Hervig, M. E., K. S. Carslaw, Th. Peter, T. Deshler, L. L. Gordley, G. Redaelli, U. Biermann, and J. M. Russell III, Polar stratospheric clouds due to vapor intrusions: HALOE observations of the Antarctic vortex in 1993, *J. Geophys. Res.*, *102*, 28,185–28,193, 1997.

Inoue, T., On the temperature and effective emissivity determination of semi–transparent cirrus clouds by bi–spectral measurements in the 10 mm window region, *J. Meteor. Soc. Japan*, *63*, 88–98, 1985.

Inoue, T., A cloud type classification with NOAA 7 split–window measurements, *J. Geophys. Res.*, *92*, 3991–4000, 1987.

Jensen, E. J., O. B. Toon, D. L. Westphal, S. Kinne, and A. J. Heymsfield, Microphysical modeling of cirrus 1. Comparison with 1986 FIRE IFO measurements, *J. Geophys. Res.*, *99*, 10,421–10,442, 1994.

Koop, T., K. S. Carslaw, and Th. Peter, Thermodynamic stability and phase transitions of polar stratospheric cloud particles, *Geophys. Res. Lett.*, *24*, 2199–2202, 1997.

Lubin, D. and D. A. Harper, Cloud radiative properties over the south pole from AVHRR infrared data, *J. Climate*, *9*, 3405–3418, 1996.

Pagan, K. L., Detection of polar stratospheric clouds over Antarctica using AVHRR satellite imagery, *M.S. Thesis*, San Francisco State University, 1996.

Parol, F., J. C. Buriez, G. Brogniez, and Y. Fouquart, Information content of AVHRR channels 4 and 5 with respect to the effective radius of cirrus cloud particles, *J. Appl. Meteor.*, *30*, 973–984, 1991.

Randall, C. E., D.W. Rusch, J.J. Olivero, R.M. Bevilacqua, L.R. Poole, J.D. Lumpe, M.D. Fromm, K.W. Hoppel, J.S. Hornstein, and E.P. Shettle, An overview of POAM II aerosol measurements at 1.06 um, *Geophys. Res. Lett.*, *23*, 3195–3198, 1996.

Roche, A. E., J. B. Kumer, and J. J. Mergenthaler, CLAES observations of CLONO2 and HNO3 in the Antarctic stratosphere, between June 15 and September 17, 1992, *Geophys. Res. Lett.*, *20*, 1223–1226, 1993.

Sassen, K., M. K. Griffin, and G. C. Dodd, Optical scattering and microphysical properties of subvisible cirrus clouds, and climatic implications, *J. Atm. Sci.*, *28*, 91,098, 1989.

Tolbert, M. A., Polar clouds and sulfate aerosols, *Science*, *272*, 1597, 1996.

Toon O. B., M. A. Tolbert, B. G. Koehler, A. M. Middlebrook, and J. Jordan, Infrared optical constants of H_2O ice, amorphous nitric acid solutions, and nitric acid hydrates, *J. Geophys. Res.*, *99*, 25,631–25,645, 1994.

Waren, S. G., Optical constants of ice from the ultraviolet to the microwave, *Appl. Optics*, *23*, 1206–1226, 1984.

Wu, M. C., A method for remote sensing the emissivity, fractional cloud cover, and cloud top temperature of high–level, thin clouds, *J. Climate Appl. Meteor.*, *26*, 225–233, 1987.

Yamanouchi, T., K. Suzuki, S. Kawaguchi, Detection of clouds in Antarctica from infrared multispectral data of AVHRR, *J. Meteor. Soc. Japan*, *65*, 949–961, 1997.